energies

MDPI

Article

CFD Prediction for Wind Power Generation by a Small Vertical Axis Wind Turbine: A Case Study for a University Campus

Yoshihide Tominaga

Wind and Fluid Engineering Research Center, Niigata Institute of Technology, Kashiwazaki 945-1195, Japan; tominaga@abe.niit.ac.jp

Abstract: The accuracy of wind power generation predicted by computational fluid dynamics (CFD) simulations combined with meteorological wind data was validated based on comparisons with directly measured data for a small vertical axis wind turbine system installed on a university campus. The CFD simulations were performed in accordance with established guidelines and frameworks for the prediction of urban wind environments. At the rooftop location, where small wind turbines are typically installed, the deviations in wind velocity from the measurements are quite large. However, in the present study, the prediction accuracy for the wind turbine site, which was 4 m above the ground, was acceptable. The total power generation estimated using the assumed power curve based on the rated output of the turbine was 56% larger than that directly measured by the power generator. However, using the power curves obtained from the measurements, the total power generation could be predicted with a high degree of accuracy and with an error of approximately 3%. It is suggested that not only the accuracy of the wind velocity but also that of the power curve is very important because they are directly related to that of the predicted power generation.

Keywords: computational fluid dynamics prediction; wind power generation; vertical axis wind turbine; case study; university campus

Citation: Tominaga, Y. CFD Prediction for Wind Power Generation by a Small Vertical Axis Wind Turbine: A Case Study for a University Campus. *Energies* **2023**, *16*, 4912. https://doi.org/10.3390/en16134912

Academic Editor: Andrey A. Kurkin

Received: 19 May 2023
Revised: 11 June 2023
Accepted: 21 June 2023
Published: 24 June 2023

1. Introduction

Wind energy is a leading renewable energy source and is expected to be used more actively in the future [1]. Large wind turbines installed on open terrains, such as offshore locations, are known for their high-power generation efficiency obtained at higher wind speeds [2]; however, there are several installation challenges, such as the huge costs and environmental impacts [3]. In addition, small wind turbines on or near buildings are expected to be utilized further to harness unused urban wind energy because of their low-noise and vibration characteristics, and their ability to convert energy efficiently into rotational energy, even at low wind speeds. This method also has the advantage of reduced power transmission losses because the locations where energy is generated and used are closer together [4]. Many reviews have been published on urban wind energy harvesting, and the challenges it faces have been summarized (e.g., [5–11]). Considerable care must be taken in selecting locations for wind turbines because the winds inside urban areas and around buildings are very complex, with high temporal and spatial variability.

Wind tunnel experiments have been used for the detailed predictions of wind-velocity distributions in urban areas [12–16]. However, few wind tunnel experiments have been used to directly explore wind energy in urban areas. Danneker and Grant [17] used wind tunnel tests to investigate wind speed measurements within the ducts around building models. Al-Quraan [18] conducted a wind energy study based on wind tunnel test results. They compared the estimated wind energy potential based on the velocity values obtained from field measurements with the predicted value based on the respective boundary layer wind tunnel data. In their results, the difference between the estimation of the wind energy potential and the calculation using the velocity from the field measurement was less than

5% for the case where the upstream terrain was homogeneous. However, in the case of inhomogeneous upstream terrain conditions, the difference increased by up to 20%. The results indicate that the accurate prediction of wind velocity is a prerequisite for the accurate prediction of wind energy potential.

Conversely, CFD simulations have been extensively used as an alternative to wind tunnel experiments. Whereas wind tunnel experiments are limited by the number of measurement points and components owing to the constraints of the measurement instruments, CFD is highly advantageous in capturing the three-dimensional distributions of wind velocity with high resolution. In particular, because digital geometry data for buildings in urban areas have recently become more readily available, it has become possible to incorporate these data into CFD to predict wind velocity distributions efficiently over a short period of time. Currently, CFD is increasingly being used in studies on the exploration of wind energy potential, and these studies have been reviewed by Toja-Silva et al. [19], Calautit et al. [20], Juan et al. [21], and Kwok and Hu [22]. Although these reviews suggest the significant potential of CFD in urban wind energy prediction, they also highlight several challenges.

A key challenge in using CFD for the prediction of wind energy in urban areas is the validation of its accuracy. The first assumption is that the wind velocity distribution must be correctly predicted. For this purpose, existing CFD guidelines and frameworks that have been developed for the prediction of wind velocity distribution around buildings and in urban areas must be useful [23–25]. Using CFD, studies have been conducted on the optimal location of wind turbines and the effects of building geometries. For simple geometries, such as those of single buildings, validation studies can be conducted with wind tunnel results with respect to mean wind velocities and their fluctuations (e.g., [26,27]). However, when actual urban areas are targeted, it is difficult to validate the accuracy of wind velocity predictions compared with that for a single building. Furthermore, a gap exists between the wind velocity and power generation predictions. Most previous studies predicted the average wind velocity using CFD and evaluated the converted power generation using wind velocity and assumed power coefficients. For example, Yang et al. [28] developed CFD-based evaluation procedures to determine potential mounting sites for wind turbines and to obtain estimates of wind power by considering the details of the local urban topography and boundary conditions of the microenvironment. In their study, the wind velocities were compared with the measurement results; however, for power generation, they only compared the wind power density (i.e., $(1/2)\rho u^3$). Nevertheless, because wind velocities are associated with long-term fluctuations, such as hourly, daily, and seasonal, in addition to turbulent fluctuations, the gap between the amount of power generation and the average wind velocity prediction is not negligible. In other words, there are very few cases in which the accuracy of the power generation prediction is directly confirmed using the measured values.

In this study, the accuracy of wind power generation predicted by CFD simulations combined with meteorological data was validated by comparing it with the directly measured accuracy for a small vertical axis wind turbine (VAWT) system installed on a university campus. The CFD simulations were performed in accordance with established guidelines and frameworks for the prediction of urban wind environments. The objectives of this study were to identify the gap between the accuracies of CFD predictions of the wind velocity field and power generation prediction, and to quantify the impact of this difference on the assessments of wind energy potential. As a result, precautions and issues that need to be considered to predict the wind power generation potential accurately can be identified for small VAWT systems installed near buildings.

The remainder of this paper is organized as follows: Section 2 introduces this study's targets and research procedure. Section 3 describes the CFD simulation conditions. Section 4 presents the simulated CFD wind velocity prediction results and their validation. Section 5 presents the power generation prediction results based on the CFD results and compares

them with the measured results. Section 6 summarizes the conclusions of this study and discusses its limitations and prospects.

2. Study's Target

2.1. Wind Turbines and the Surrounding Environment

The Niigata Institute of Technology campus, where the VAWT targeted in this study was installed, is located in Kashiwazaki City, Niigata Prefecture, Japan. Figure 1 shows an aerial view of the campus surroundings. Campus buildings were built on a hillside and are surrounded by rice paddies and woods. The Automated Meteorological Data Acquisition System (AMeDAS) station of the Japan Meteorological Agency is located approximately 2.7 km away in the northwest direction. An overview of the campus buildings is illustrated in Figure 2. The locations of the wind turbines are also indicated in Figure 2. In this study, the data obtained by the two anemometers shown in Figure 2 were used: one on the rooftop and the other near the VAWT. The anemometer installed on the rooftop is a compact weather station developed by Meisei Electric Co., Ltd. (Isesaki, Japan) [29]. The wind velocity and direction were measured using an ultrasonic anemometer at the height of 4 m above the rooftop floor, as shown in Figure 2a. The observation data transmitted at 1 min intervals from the weather station were accumulated in a leased cloud server automatically and in real-time. Ten minute average wind direction and wind velocity were calculated from the accumulated data. The wind velocity and direction near the VAWT were measured using a wind sentry anemometer and vane (Model 03002L, R.M. Young Co., Traverse, MI, USA) at the height of 4 m above the ground, as shown in Figure 2b. The output data from the anemometer were transmitted at 30 s intervals from a data logger (RTR505B, T&D Co., Matsumoto, Japan) to the cloud server, and 1 h average values were calculated. The VAWT system consisted of three Kharios N1000-BGGs manufactured by Nakanishi Metal Works Co., Ltd (Osaka, Japan). The number of blades was four, the length was 2.5 m, the rotating diameter was 1.5 m, and the height of the upper end of the vane was 6.8 m. The VAWT was designed with a starting wind speed of 0.8 m/s, cut-in wind speed of 2.0 m/s, and power generation of 1000 W at 13 m/s.

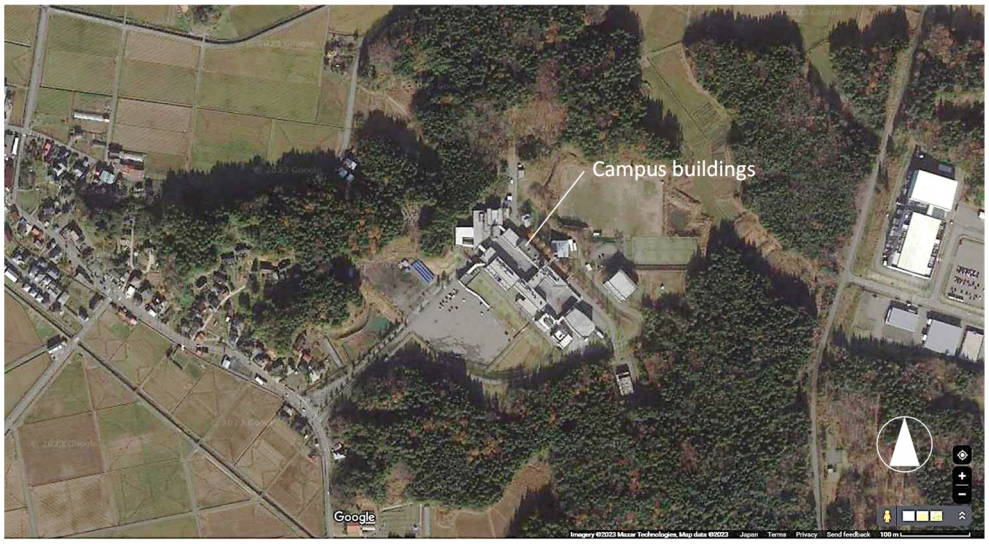

Figure 1. Aerial view of the campus surroundings (©Google Maps).

Observations and measurements were made for 4 years from 2017 to 2021. Only the data for the winter period (December to March) were used because the wind is relatively strong, owing to the monsoon blowing from the Sea of Japan in this area; accordingly, the thermal effect is small. Additionally, only data that were associated with the conditions based on which the 10 min averaged velocity at the meteorological station exceeded 2 m/s were retained in an attempt to exclude measurement values affected by the thermal

effect. The frequency of occurrence and average wind speed for each wind direction at the meteorological station during the observation period are shown in Figure 3. The wind directions with the largest frequencies of occurrence were W, WNW, and SE, but strong winds were limited to the westward direction owing to the monsoon.

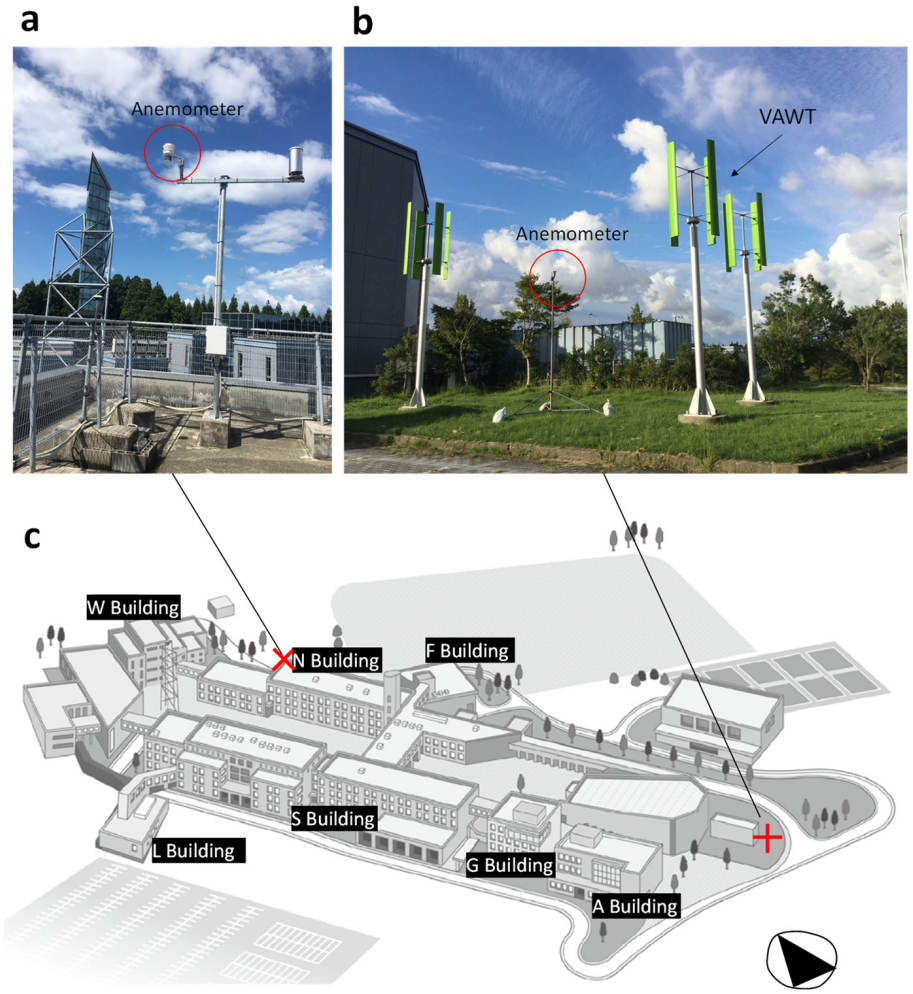

Figure 2. Anemometer on the rooftop (**a**), near vertical axis wind turbine (**b**), and schematic overview of the campus buildings (**c**).

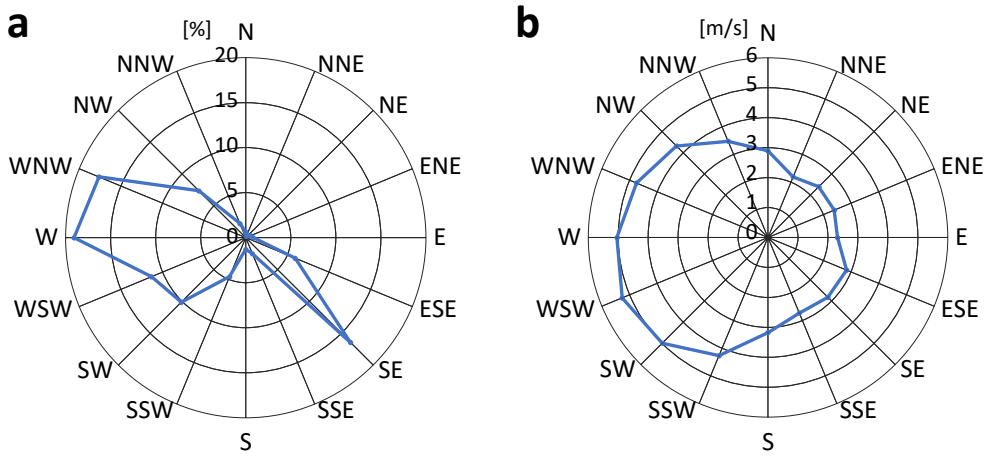

Figure 3. Occurrence frequency of wind direction (**a**) and mean wind velocities (**b**) for 16 wind directions at the meteorological station (AMeDAS Kashiwazaki).

2.2. Research Procedure

An outline of the CFD simulations performed in this study is shown in Figure 4. Campus buildings and topographic undulations were reproduced in the CFD simulations as described subsequently in detail, but not the VAWT itself. The wind velocity ratio was calculated as the ratio of the wind velocity at the VAWT location to the reference wind velocity at the meteorological station. For comparison, the wind velocity ratio was also calculated on the rooftop of a building, which is typically selected as the setting location for small wind turbines. That is, the following wind velocity ratios on the rooftop (*RT*) and in the vicinity of the VAWT (*WT*) were calculated for each wind direction (*i*) and used to validate the CFD simulations.

$$R_{RT\_i} = \frac{V_{RT\_i}}{V_{Met\_i}} \quad (1)$$

$$R_{WT\_i} = \frac{V_{WT\_i}}{V_{Met\_i}} \quad (2)$$

where R_{RT_i} and R_{WT_i} are the velocity ratios at the *RT* and *WT* locations, respectively. V_{RT_i} and V_{WT_i} are the velocities at the *RT* and *WT* locations, respectively. V_{Met_i} is the velocity at the meteorological station; in the CFD simulations, it was replaced by the velocity at the inlet boundary at the same height. In this study, the calculations were performed separately for 16 wind directions and the wind velocity ratios for each wind direction, i.e., R_{RT_i} and R_{WT_i}, were stored. The changes in wind direction were considered by multiplying the directional wind velocity ratios with the directional wind velocities according to the wind directions at the meteorological station on an hourly basis. It should be noted that the wind directions at the meteorological station and the inlet boundary of the CFD simulation were assumed to be identical.

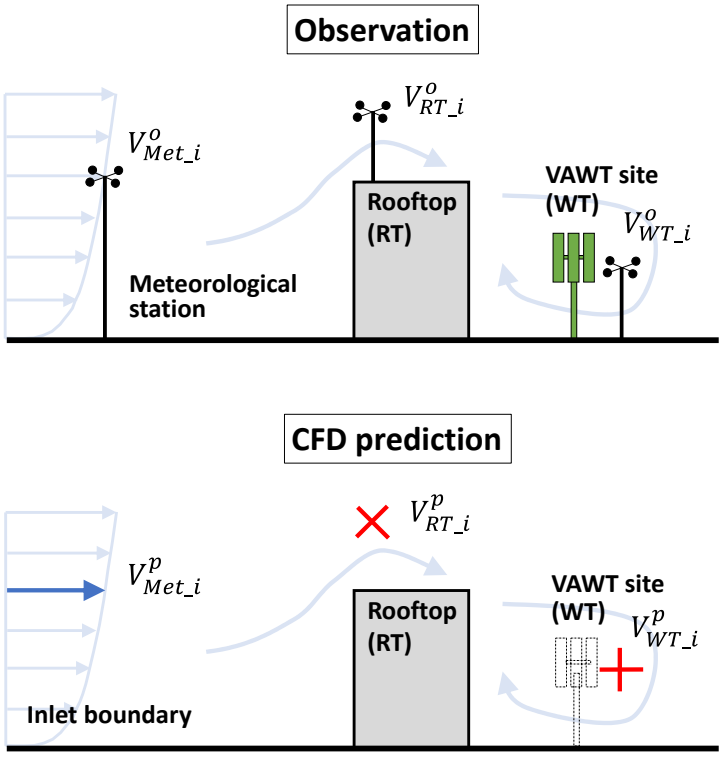

Figure 4. Schematic comparing the observation and CFD setups.

The power generation prediction procedure is shown in Figure 5. The input condition was the hourly variation in wind velocity and direction at the meteorological station. Multiplying them by the aforementioned wind velocity ratio at the WT location obtained by CFD for each wind direction yielded the hourly wind velocity variation expressed by

Equation (2). The temporal variation in the power generation by the VAWT can be predicted by multiplying this wind velocity variation by the power curve of the VAWT. The power curve used in this process was validated based on the observed results. Finally, the total power generation for a given period was predicted by integrating the hourly variations in power generation. The amount of power generated during this period was also validated.

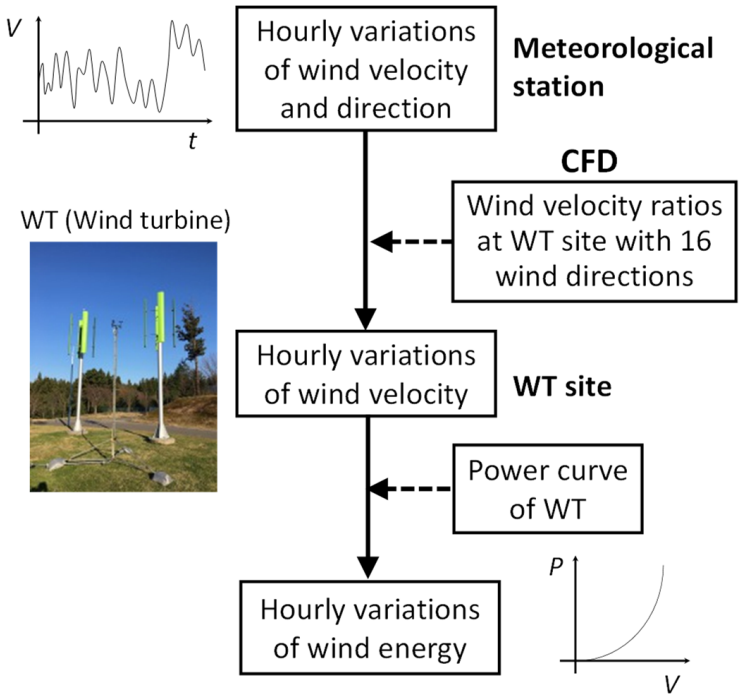

Figure 5. The procedure of power generation prediction.

3. CFD Simulation Setup

3.1. Computational Model and Domain

Based on the best practice guidelines [23,24], an 800 m × 800 m × 200 m computational domain centered on campus buildings was created, as shown in Figure 6. Because the same computational domain was used for 16 wind directions, the horizontal domain size was determined so that the downstream domain length is adequately long to allow the development of the wake region behind the buildings, which is beneficial for the simulation convergence. The domain height is over 10 times the height of the highest building, which is adequately large to ensure that the blocking ratio is small enough. Considering the practical costs of data preparation and computational burdens, only campus buildings were explicitly reproduced, whereas other land features, such as trees and small obstacles, were modeled using roughness parameters. The topographic undulations were also reproduced based on 5 m mesh data from the Digital National Land Information provided by the Geospatial Information Authority of Japan. Three-dimensional geometric data were obtained from the retrieved point cloud data.

3.2. Computational Grid

The computational grid used in this study was confirmed to be grid independent according to a grid sensitivity analysis. The basic computational grid consisted of 2,257,401 tetrahedral and pyramidal cells. The boundary layer cells were set up on the ground surface [24]. The smallest cell volume was 5.2×10^{-5} m^3, and the largest was 2.1×10^{-3} m^3. The horizontal resolutions of the ground surface and buildings were 1.6 m and 1.0 m, respectively. The horizontal resolution of the region outside the campus was 15.0 m for all grids. The same computational grid was used to perform the CFD simulations for 16 wind directions.

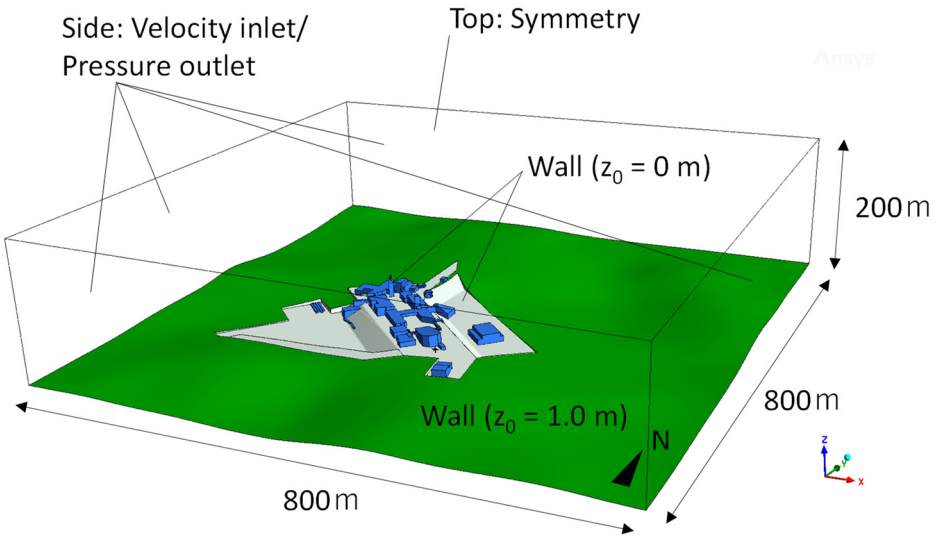

Figure 6. Computational domain and boundary conditions used in this study.

Two different grids, fine and coarse, were prepared for grid sensitivity analysis. The main grid features are summarized in Table 1. The three grids on the campus buildings and ground surfaces are compared in Figure 7.

Table 1. Main features of the grid adopted for the grid sensitivity study.

Grid	Total Number of Cells	Smallest Cell Volume (m^3)	Largest Cell Volume (m^3)	Resolution of Ground Surface (m)	Resolution of Building Surface (m)
Coarse	1,375,619	1.3×10^{-5}	2.5×10^{-3}	2.0	1.5
Medium	2,257,401	5.2×10^{-5}	2.1×10^{-3}	1.6	1.0
Fine	5,377,799	3.1×10^{-5}	2.1×10^{-3}	1.6	0.5

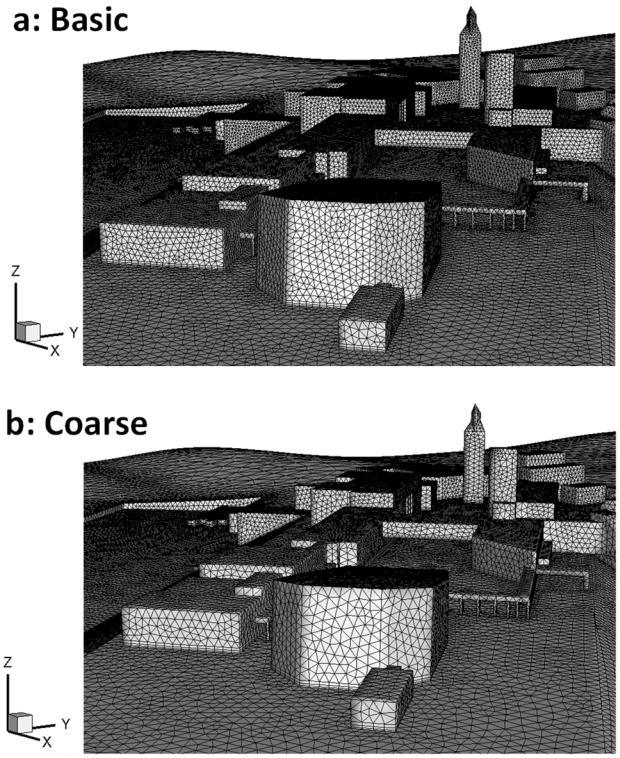

Figure 7. *Cont.*

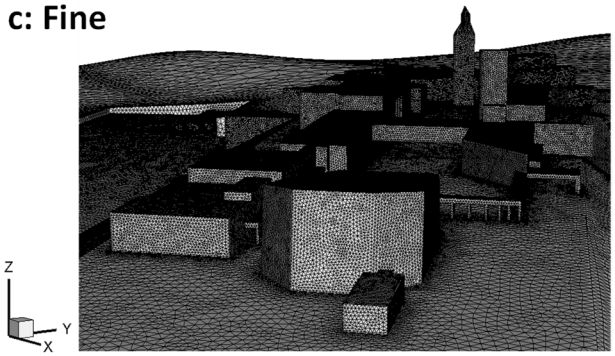

Figure 7. Computational grids for grid sensitivity analysis: (**a**) basic grid with 2,257,401 cells, (**b**) coarse grid with 1,375,619 cells, and (**c**) fine grid with 5,377,799 cells.

3.3. Solver Settings

The governing equations for the mass and momentum were solved using the finite volume approach of ANSYS Fluent 2022R1 [30]. CFD simulations were performed for neutral atmospheric boundary layers and isothermal conditions under a steady state. The Reynolds-averaged Navier–Stokes equations (RANS) (mass and momentum conservation) for incompressible fluids without body forces were used:

$$\frac{\partial U_i}{\partial x_i} = 0 \tag{3}$$

$$\frac{\partial (U_i U_j)}{\partial x_j} = -\frac{1}{\rho}\frac{\partial P}{\partial x_i} + \frac{\partial}{\partial x_j}\left(\nu \frac{\partial U_i}{\partial x_j} - \rho \overline{u_i' u_j'}\right) \tag{4}$$

where P is the mean pressure, ρ the fluid density, and ν is the kinematic viscosity. Using the two-equation RANS approach, the Reynolds stresses ($\overline{u_i' u_j'}$) are prescribed in terms of the mean flow values, and the statistical turbulence closure (turbulence kinetic energy and turbulence dissipation rate equations) is based on the Boussinesq hypothesis, i.e., a linear relationship between the turbulent stresses and the mean velocity gradients,

$$-\overline{u_i' u_j'} = 2\nu_t S_{ij} - \frac{2}{3} k \delta_{ij} \tag{5}$$

where S_{ij} is the strain rate tensor ($= \frac{1}{2}\left(\frac{\partial U_i}{\partial x_j} + \frac{\partial U_j}{\partial x_i}\right)$), ν_t is the kinematic eddy viscosity, δ_{ij} the Kronecker Delta function, and k is the turbulence kinetic energy (TKE). The kinematic eddy viscosity is modeled as follows,

$$\nu_t = C_\mu \frac{k^2}{\varepsilon} \tag{6}$$

In this study, a realizable k–ε turbulence model [31] was used. The modeled transport equations for TKE and the turbulence dissipation rate (ε) in the realizable k–ε model are,

$$\frac{\partial U_j k}{\partial x_j} = \frac{\partial}{\partial x_j}\left[\left(\nu + \frac{\nu_t}{\sigma_k}\right)\frac{\partial k}{\partial x_j}\right] + P_k - \varepsilon \tag{7}$$

$$\frac{\partial U_j \epsilon}{\partial x_j} = \frac{\partial}{\partial x_j}\left[\left(\nu + \frac{\nu_t}{\sigma_k}\right)\frac{\partial \epsilon}{\partial x_j}\right] + C_1 \frac{\varepsilon}{k} P_k - C_2 \frac{\varepsilon^2}{k + \sqrt{\nu \varepsilon}} \tag{8}$$

where $\sigma_k = 1$, $\sigma_\varepsilon = 1.2$, and $C_2 = 1.9$.

The production of k is modeled as follows,

$$P_k = \nu_t S^2,\ S = \sqrt{2S_{ij}S_{ij}} \tag{9}$$

The model coefficient C_1 is determined as follows,

$$C_1 = max\left[0.43, \frac{\eta}{\eta+5}\right],\ \eta = S\frac{k}{\varepsilon} \tag{10}$$

In contrast to the standard k–ε model [32], C_μ in Equation (6) is not constant and is computed from

$$C_\mu = \frac{1}{A_0 + A_S\frac{kU^*}{\epsilon}},\ U^* \equiv \sqrt{S_{ij}S_{ij} + \Omega_{ij}\Omega_{ij}},\ \Omega_{ij} = \frac{1}{2}\left(\frac{\partial U_i}{\partial x_j} - \frac{\partial U_j}{\partial x_i}\right) \tag{11}$$

The model constants A_0 and A_S are given by

$$A_0 = 4.04,\ A_s = \sqrt{6}cos\phi \tag{12}$$

$$\phi = \frac{1}{3}cos^{-1}\left(\sqrt{6}W\right),\ W = \frac{S_{ij}S_{jk}S_{ki}}{\widetilde{S}^3},\ \widetilde{S} = \sqrt{S_{ij}S_{ij}} \tag{13}$$

The superiority of the realizable k–ε model over other k–ε turbulence models has been reported in previous systematic validation studies for flow around buildings [33–36]. Notably, Yang et al. [28] concluded that the realizable k–ε model provides more reasonable predictions of the turbulence intensity for the simulations of the swirling and separating flows around buildings than those with the use of the standard and RNG k–ε models according to their CFD simulations and field measurements conducted to evaluate the wind resources available in an urban area.

The advection terms for the transport equations were discretized using a second-order upwind scheme for momentum and a first-order upwind scheme for k and ε, and the pressure interpolation was maintained at the second order. The semi-implicit method for the pressure-linked equations (SIMPLE) algorithm was used for the pressure–velocity coupling. Convergence was assumed to be obtained when all scaled residuals leveled off and reached a minimum of 10^{-5} for x, y, and z momentum and 10^{-4} for k, ε, and continuity. Approximately 30 min per wind direction was required for the convergence on a computer equipped with an Intel® Core™ i3-8100 CPU@3.60 GHz processor.

3.4. Boundary Conditions

The wind velocity profiles of the approaching flow were classified as roughness category II, as specified in the AIJ Recommendations for Loads on Buildings of the Architectural Institute of Japan [37].

$$U(z) = U_S\left(\frac{z}{z_S}\right)^\alpha \tag{14}$$

where U_S is the velocity at reference height, z_S, and α is the power law exponent (=0.15).

The TKE (k) was estimated from the following equation using the turbulence intensity in the streamwise direction, I_u, based on the AIJ guidelines [24].

$$k(z) = (I_u(z)U(z))^2 \tag{15}$$

$$I_u(z) = \frac{\sigma_u(z)}{U(z)} = 0.1\left(\frac{z}{z_G}\right)^{(-\alpha-0.05)} \tag{16}$$

where σ_u is the standard deviation of velocity fluctuation in the streamwise direction, and z_G is the boundary layer height (=350 m).

The profile of the dissipation rate of the TKE, ε, is given by Equation (17) based on the AIJ guidelines.

$$\varepsilon(z) = C_{\mu}^{\frac{1}{2}} k(z) \frac{U_S}{Z_S} \alpha \left(\frac{z}{Z_S} \right)^{\alpha - 1} \quad (17)$$

where C_{μ} is a model constant (=0.09).

Table 2 presents the boundary conditions imposed at each boundary of the simulation domain. In this study, the wind velocities at specific locations were predicted using wind velocity ratios, i.e., based on Equations (1) and (2) and the velocity measured by the meteorological station. In the practical range of wind velocities, the effect of the Reynolds number was considered to be very small; therefore, the reference wind velocity at which the simulations were performed can be ignored. In this study, the wind velocity was set at 4.0 m/s at the measurement height of the meteorological station considering the average wind velocity in the area concerned during the observation period. The vertical profiles of the average streamwise wind velocity and TKE imposed at the inlet boundary are shown in Figure 8. In this study, calculations were performed for 16 wind directions within the same computational domain, as shown in Figure 6. For wind directions perpendicular to the computational domain, the inlet boundary conditions were given as distributions based on Equations (14)–(17), and the sides were modeled as a symmetry wall (zero normal velocity and zero normal gradients of all variables). A static pressure of zero was imposed at the opposite outlet. However, when the wind direction was oblique to the computational domain, the velocity profiles (divided into x and y components according to the wind direction) were given at the two side planes. In this case, zero static pressures were imposed on the two opposite planes at the outlet. The top part of the computational domain was modeled as a symmetrical wall for all wind directions.

Table 2. Boundary conditions imposed at each boundary of the domain.

Boundary	Boundary Conditions
Inlet	Imposed vertical profiles for U with Equation (14), k with Equation (15), and ε with Equation (17) (Velocity inlet)
Outlet	Zero gradients for U, k, and ε. Zero for P (Pressure outlet)
Sides	Zero gradient conditions for all variables with the exception that the normal components of velocity with respect to the boundaries are set to zero (Symmetry)
Top	Symmetry condition
Ground (Outside)	Standard wall function with the sand grain-based roughness modification (Wall) with k_S = 0.98 m, C_S = 10.0
Ground (Inside)	*Wall* condition with k_S = 0
Building	*Wall* condition with k_S = 0

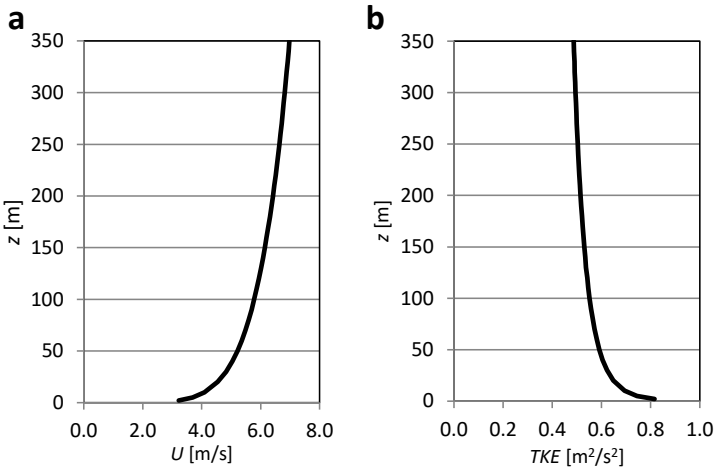

Figure 8. Vertical profiles of the averaged streamwise velocity (**a**) and turbulence kinetic energy (TKE) (**b**).

The standard wall functions of Launder and Spalding [38] were used with the sand grain-based roughness modification of Cebeci and Bradshaw [39]. The parameters k_S and C_S in the roughness modification in Fluent were determined from their relationship with the aerodynamic roughness length z_0 [40],

$$k_S = \frac{9.793 z_0}{C_S} \tag{18}$$

For the region outside the campus, where trees and other small obstructions were implicitly modeled, k_S was set to 0.98 m and C_S = 10.0 for z_0 = 1.0 m. The ground in the campus area and building surfaces were set to a zero roughness height (k_S = 0).

4. CFD Simulation Results for Wind Velocity Prediction

4.1. Grid Sensitivity Analysis

For the W wind direction, the wind velocity and directions were sampled at 25 × 25 points with 10 m intervals over an area of 250 m × 250 m around the campus buildings at the WT height in the two grid cases with different resolutions. A comparison of the scatter plots is shown in Figure 9. As shown in Figure 9a,c, the differences between the basic and fine grids were very small for both the wind velocity and wind direction, except for a few outliers. However, as shown in Figure 9b,d, the differences between the basic and coarse grids were larger, especially in the lower wind velocity region. These results indicate that the resolution of the basic grid was adequate. Therefore, the calculations for all 16 wind directions were performed by using this basic grid.

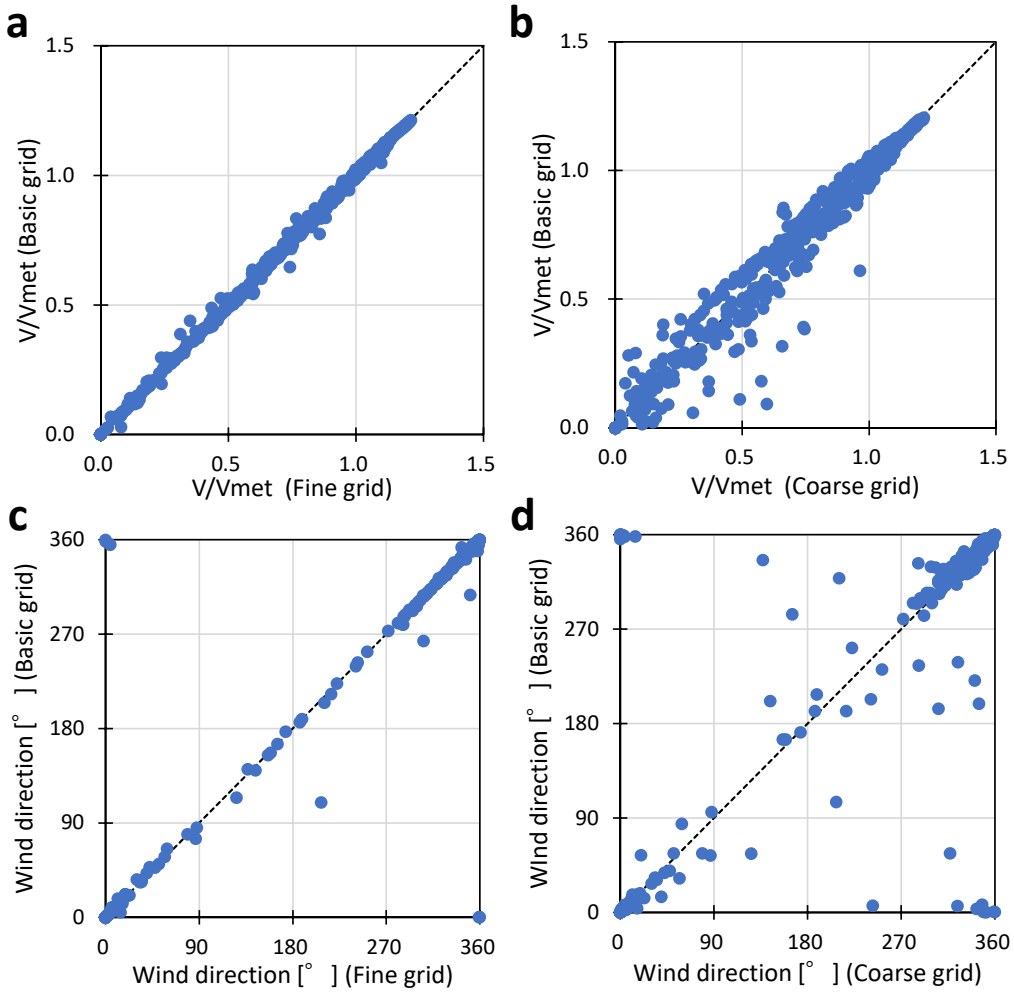

Figure 9. Grid sensitivity analysis based on predicted wind velocities and directions.

4.2. General Flow Pattern

As an example of the predicted wind velocity field for the two wind directions W and SE, which occur most frequently, Figure 10 illustrates the horizontal distributions of the mean streamlines and the velocity magnitude at the two different heights, i.e., the WT height (4.0 m above the campus ground level) and the RT height (4.0 m above the roof height of N Building) (Figure 2). The WT location is indicated by the symbol "+" and the RT location by the symbol "×." The velocity values were normalized using V_{Met}, that is, the values represent the velocity ratios.

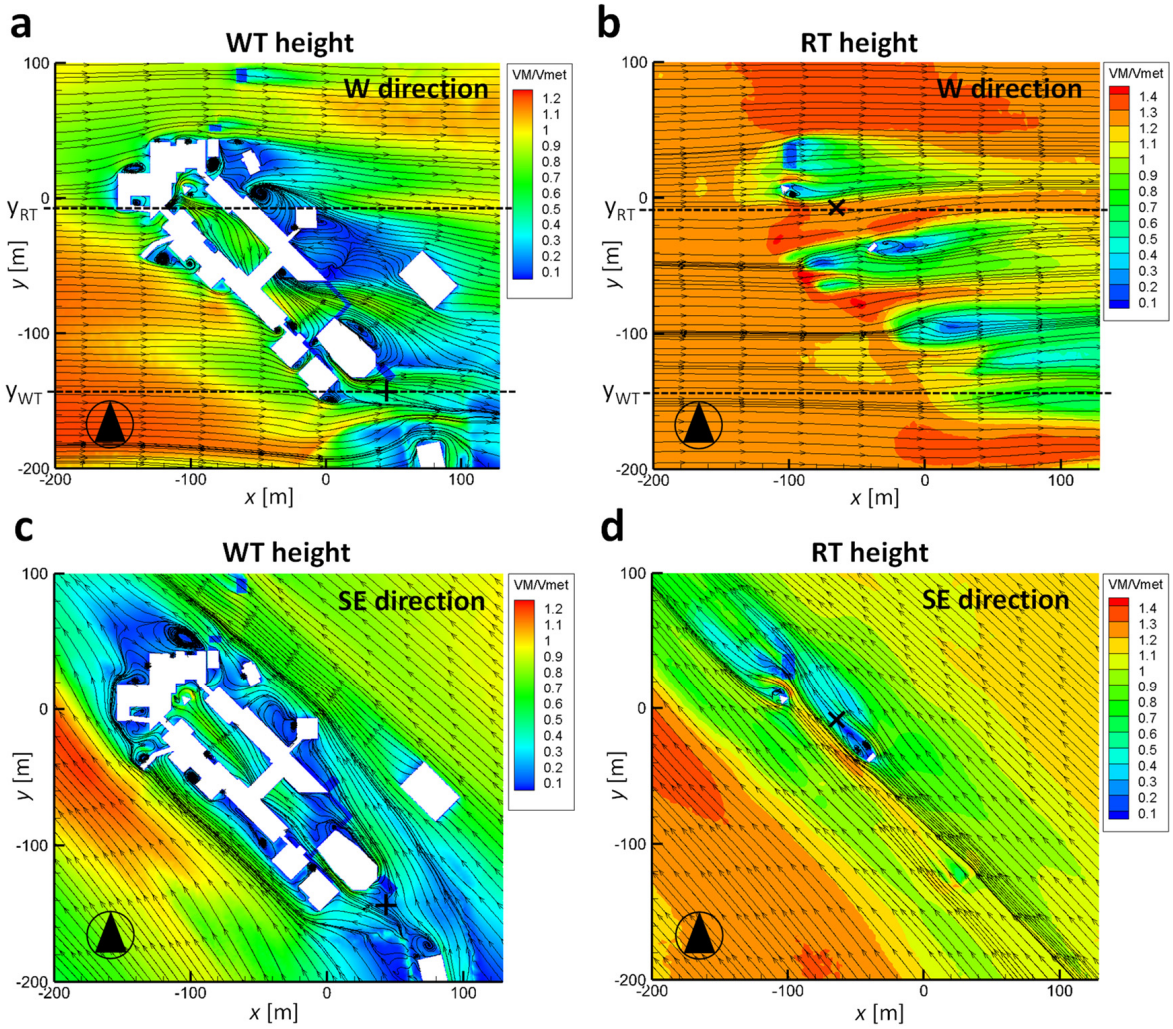

Figure 10. Horizontal distributions of streamlines and wind velocity at two wind directions (W, SE) at two different heights (WT and RT).

The results for the W wind direction are shown in Figure 10a,b. At the WT height (Figure 10a), the wind velocity ratio was relatively high in the campus area and was approximately 0.8 because the upwind side was generally open. This area was directly affected by the flow separated from the building on the NW side. At the RT height (Figure 10b), the wind velocity ratio was large (approximately 1.3) because of the effect of the flow acceleration at the roof of the upwind building (S building) (Figure 2). The results for the SE wind direction are shown in Figure 10c,d. At the WT height (Figure 10c), the wind velocity ratio was weak and approximately equal to 0.4 because the terrain on the upwind side was slightly heaving, and an upwind building existed. At the RT height (Figure 10d), the wind velocity ratio was also low (approximately 0.4) because it was located in the wake region of the windward tower.

Figure 11 compares the vertical distribution of the streamlines and velocity magnitude for the W wind direction with the TKE distributions. The locations of the section planes are shown in Figure 10a,b, respectively. Figure 10 shows the RT and WT locations. Figure 11a,b show the distributions of the wind velocity and TKE at the section plane across the RT location. The velocity at the RT location was strongly affected by the separation flow that occurred on the roofs of the upwind and its own building. Figure 11b shows that the TKE value exhibits a large peak near the RT location. This implies that large velocity fluctuations occurred [41]. The results at the section plane across the WT location are shown in Figure 11c,d. The WT location was relatively far from the upwind building, and both the wind velocity and TKE were affected by a smaller degree by the upwind building.

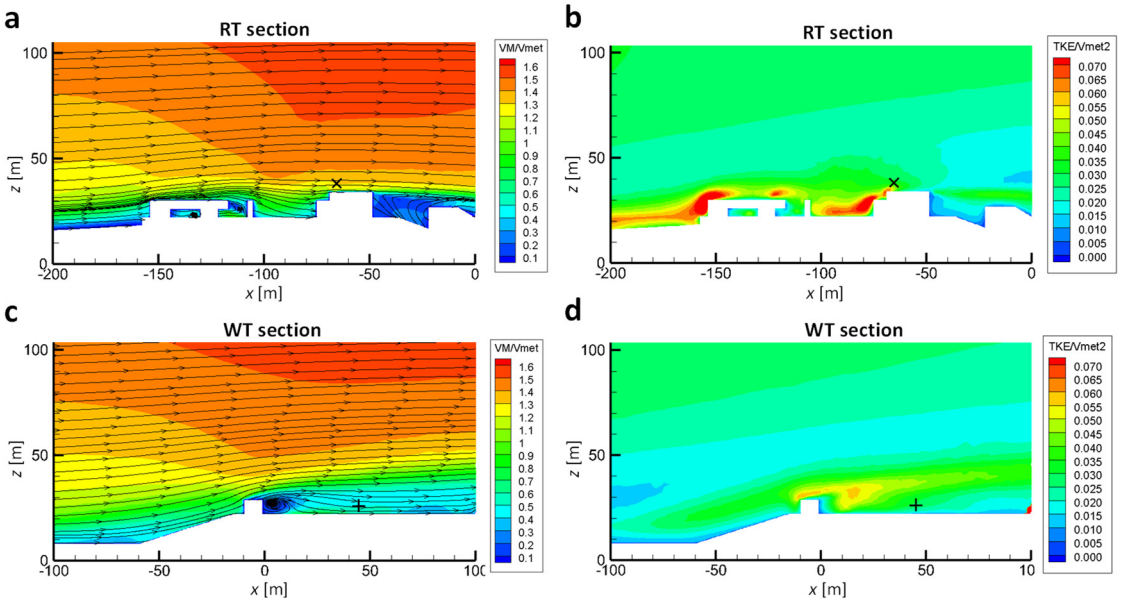

Figure 11. Mean streamlines and wind velocity (**a**,**c**) and TKE (**b**,**d**) at vertical sections across the RT and WT locations.

4.3. Validation of Velocity Fields

Figure 12a,b show a comparison of the observed and predicted wind velocity ratios at the RT (a) and WT (b) locations for each wind direction. For the RT location, the wind velocity ratio was overestimated for many wind directions, whereas some wind directions, such as SW, were underestimated. The larger wind speed ratio is attributed to the fact that the effect of the surrounding trees is only considered as a roughness parameter, which results in a smaller deceleration effect. The reason for the difference in the wind velocity ratio in the W direction is attributed to the fact that the separation flow around the upwind building was not accurately reproduced in the region near the RT location. It is well known that the steady-state RANS calculations used in this study cannot accurately predict the separation and recirculation flows [42–45]; this indicates that the accurate prediction of wind velocities on rooftops is quite challenging. Toja-Silva et al. [26] extensively investigated the prediction accuracy of the separation flows around the roof of a single building using various RANS turbulence models. Their results suggested that there were inherent deviations from the experimental results, although the choice of turbulence model provided some improvement in accuracy. However, at the WT location shown in Figure 12b, the overall trend was well reproduced; that is, the values on the NE and SW sides were larger, and those on the NW and SE sides were smaller. Although the wind velocity ratio predicted by the CFD was larger in the wind directions from NE to E, the occurrence frequencies in these wind directions were low. The smaller measurement values may also be due to the fact that the anemometer at the WT location was placed in a position

surrounded by the wind turbines, which is in their wake region, thus resulting in weaker wind velocity measurements [46,47].

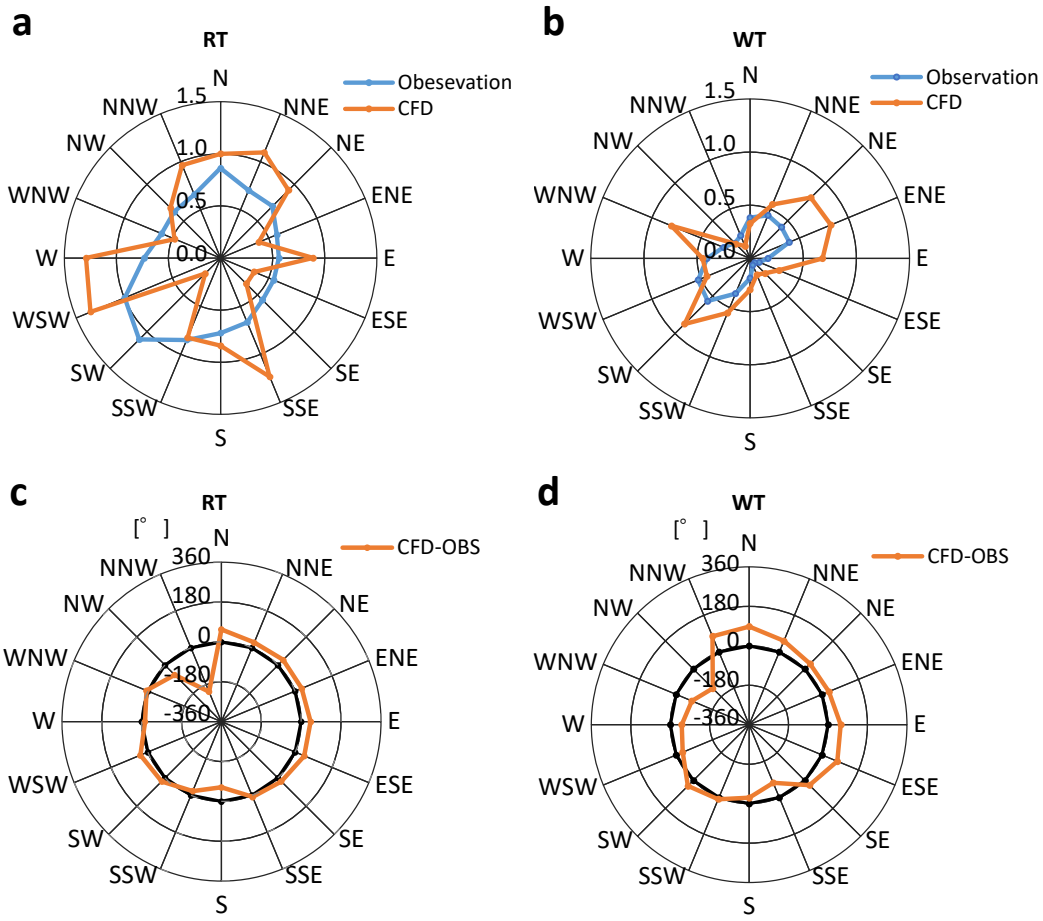

Figure 12. Comparison of wind velocity ratios and directions between observations and CFD predictions at the RT (**a**,**c**) and WT (**b**,**d**) locations.

The predicted and measured wind directions at the RT and WT locations for each incident wind direction are compared in Figure 12c,d. The orange lines indicate the difference between the two, and the black lines indicate that the difference is 0°; that is, both are perfectly aligned. At the RT location (Figure 11c), although the agreement was generally good, the predicted wind directions exhibited large deviations in the NW and NNW directions. This could be due to the effects of separation flow on the roofs of the upwind buildings. This deficiency can be improved by the use of a higher-order turbulence model, such as the Large Eddy Simulation (LES). At the WT location (Figure 11d), the agreement was somewhat worse than that of the rooftop, particularly for wind directions from NNW to SE. This may be because the effects of obstructions, such as trees located on the upwind side for these wind directions, were not properly considered.

In summary, at the RT location, the deviation in the CFD results from the measured velocity ratios was very large, although the accuracy of the wind directions was acceptable. This indicates that the prediction of wind velocity near the rooftop, where wind turbines are typically installed, is challenging. However, at the WT location, the tendency of the wind velocity distribution was captured well, although it was not perfect. The agreement between wind velocity ratios did not necessarily correspond to the agreement between wind directions. This is because the airflow around buildings is less difficult to predict compared with the separation flows around roofs. This result is consistent with the high accuracy of the overall prediction of the pedestrian wind environment, even if the CFD was based on the RANS model (e.g., [48]).

5. Prediction of Wind Power Generation

It is important to use accurate power curves to predict wind power generation (e.g., [49,50]). Although power curves are typically provided by manufacturers, their accuracy and universality remain unclear. The hourly averaged wind velocity measured at the WT location and hourly integrated power generation for the same period are plotted in Figure 13. For this VAWT, the manufacturer did not disclose the power curve of the generator; therefore, an approximate power curve was created such that an output of 1 kW at a wind speed of 13 m/s was set for each turbine generator, which is the rated output of the wind turbine, and the power generation was assumed to be proportional to the cube of the wind velocity at the lower velocities. This power curve is shown as a black-dotted line in Figure 13 and is expressed by the following function,

$$P = 0.0014 V_{WT}^3 \tag{19}$$

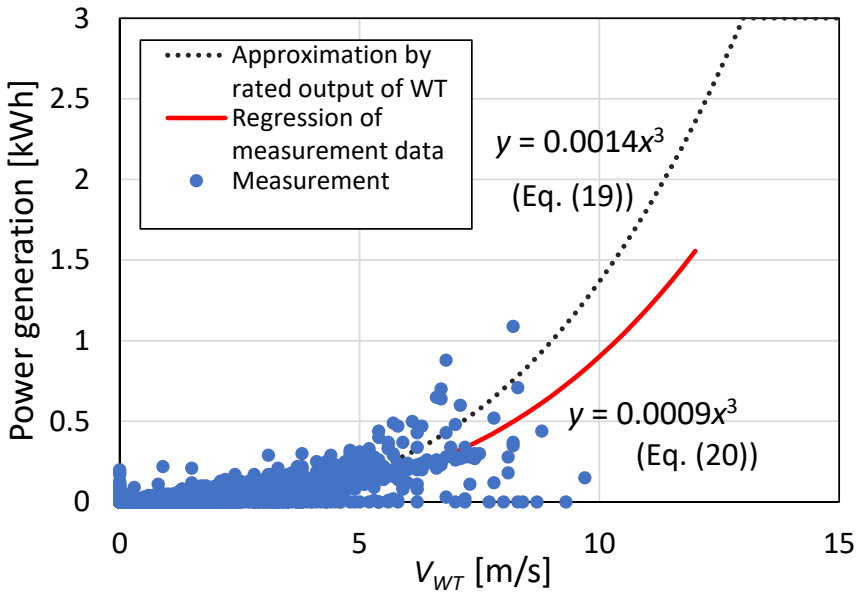

Figure 13. Power generation curves obtained by approximating the rated output of WT and regression of measurement data.

Based on the assumption that power generation is proportional to the cube of the wind velocity, the red regression line is obtained using the measured values and expressed according to the following function,

$$P = 0.0009 V_{WT}^3 \tag{20}$$

Compared with the power curve obtained from the rated output (Equation (19)), the generated power obtained from the actual measurements (Equation (20)) was approximately 64%, which is considerably smaller. This is because the actual wind velocities fluctuate extensively, and these power curves do not consider these effects. In other words, the use of the power curve obtained from the rated output may considerably overestimate the actual power generation.

Figure 14 shows a comparison of the total power generation accumulated over the entire observation period based on the method described in Figure 5. If Equation (19) (obtained from the rated output) was used, the total power generation was overestimated by 56% compared with the measured value. This is evident from the differences in the power curves in Figure 13. However, the power generation values obtained using Equation (20) are predicted with an error of 3%, which is very accurate. This indicates the importance of accurately estimating the power curve. As an example, Figure 15 shows the results of the comparison of daily integrated power generation for one winter season. The results

were compared with those predicted using Equations (19) and (20). Both prediction results accurately captured the daily variation in power generation; however, they overestimated or underestimated the amount of power generated from day to day. The degree of overestimation is smaller when Equation (20) is used. It should be noted that the predicted value (as an integrated value) is close to the observed value as a result of offsetting these daily errors, and the error would be even larger and not negligible if the daily power generation had to be accurately predicted. As pointed out by Jung and Broadwater [51], the use of the certified manufacturer power curves does not guarantee accurate conversions from the wind speed to the wind power forecast. There are two possible causes: uncertainty of input wind speeds including its turbulence nature and oversimplification of the power curve [49,50]. It is necessary to clearly separate the two causes and then seek a way to identify a way to construct a more effective power curve.

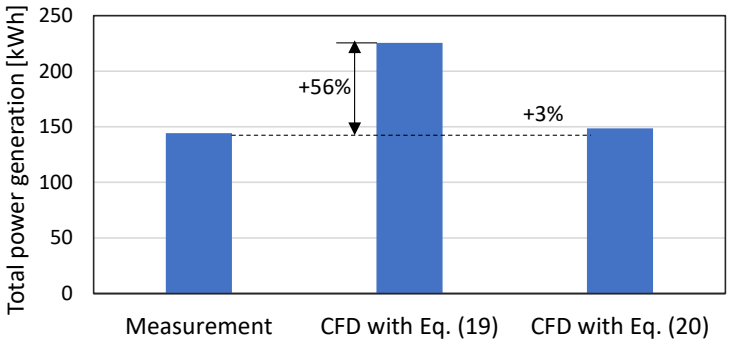

Figure 14. Comparison of total power generations measured and estimated by CFD using different power curves.

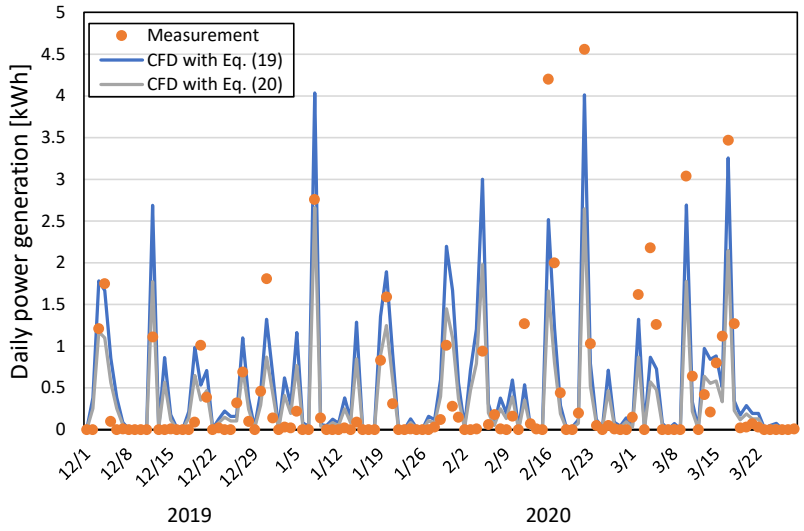

Figure 15. Comparison of daily power generations measured and estimated by CFD using different power curves.

6. Conclusions

The accuracy of wind power generation predicted by CFD simulations combined with meteorological wind data was validated for a small VAWT system installed on a university campus. This study's conclusions are summarized as follows:

- At the rooftop location, where wind turbines were typically installed, the wind velocity ratio was overestimated in many wind directions, but it was significantly underestimated in some wind directions. Because the wind velocities at the rooftop location were affected considerably by the separation flows caused by the roofs of the upwind

buildings and their own buildings, it is challenging to predict accurately these flows in steady-state RANS calculations, which are often used in practical applications;
- Although the reproduction of the surrounding trees remains to be considered, wind velocity distributions near the ground were found to be more accurate than those on the rooftop. This result is consistent with the relatively high accuracy of the overall prediction of the pedestrian wind environment, even when the CFD is based on the RANS model;
- Compared with the power curve assumed based on the rated output, that obtained from the measurement results was approximately 64% smaller. This indicates that the power curve assumed from the rated output may have considerably overestimated power generation;
- Because the accuracy of the power curve is directly related to the accuracy of the power generation prediction, considerable care must be exercised during its selection. However, using the power curves obtained from the measurements, the integrated values for the entire observation period were predicted with a high degree of accuracy and with an error of approximately 3%;
- The accurate prediction of the integrated values is the result of offsetting daily errors, which would be even larger and not negligible if the daily generation had to be accurately predicted; We recognize that it is worth reporting this outcome. However, this study has the following limitations that should be considered in future research;
- This study only included data from the snowy winter period. Accordingly, accurate predictions of wind power generation throughout the entire season will be a future challenge;
- To improve the prediction accuracy of the wind velocity distribution at the rooftop, a higher-order turbulence model, such as LES, can be used. Additional studies are needed to determine the difference in accuracy depending on the choice of the turbulence model;
- However, obtaining accurate power curves in advance is difficult. If CFD is used to predict the wind energy potential, it is necessary to establish a methodology and formulation to determine accurately the power curves of wind turbines. There are two possible causes for this inaccuracy: uncertainty of input wind speeds, turbulence nature, and oversimplification of the power curve. It is necessary to clearly separate the two causes and then seek a way to identify a way to construct a more effective power curve.

Funding: This research received no external funding.

Data Availability Statement: Data will be made available on request.

Acknowledgments: The author thanks Atsuki Yamazaki, a former undergraduate student, and Takahiro Suzuki, a technical staff member at the Wind and Fluid Engineering Research Center at the Niigata Institute of Technology, for their invaluable assistance with the CFD modeling and simulations. The author would also like to thank Fumiko Ibe, a member of the Wind and Fluid Engineering Research Center, for her significant contribution to the preparation of this manuscript.

Conflicts of Interest: The author declares no conflict of interest.

References

1. REN21. *Renewables 2022 Global Status Report*; REN21 Secretariat: Paris, France, 2022.
2. Barooni, M.; Ashuri, T.; Sogut, D.V.; Wood, S.; Taleghani, S.G. Floating Offshore Wind Turbines: Current Status and Future Prospects. *Energies* **2022**, *16*, 2. [CrossRef]
3. Galparsoro, I.; Menchaca, I.; Garmendia, J.M.; Borja, Á.; Maldonado, A.D.; Iglesias, G.; Bald, J. Reviewing the ecological impacts of offshore wind farms. *NPJ Ocean Sustain.* **2022**, *1*, 1. [CrossRef]
4. Chaudhary, G.; Lamb, J.J.; Burheim, O.S.; Austbø, B. Review of Energy Storage and Energy Management System Control Strategies in Microgrids. *Energies* **2021**, *14*, 4929. [CrossRef]
5. Walker, S.L. Building mounted wind turbines and their suitability for the urban scale—A review of methods of estimating urban wind resource. *Energy Build.* **2011**, *43*, 1852–1862. [CrossRef]

6. Toja-Silva, F.; Colmenar-Santos, A.; Castro-Gil, M. Urban wind energy exploitation systems: Behaviour under multidirectional flow conditions—Opportunities and challenges. *Renew. Sustain. Energy Rev.* **2013**, *24*, 364–378. [CrossRef]
7. Micallef, D.; van Bussel, G. A Review of Urban Wind Energy Research: Aerodynamics and Other Challenges. *Energies* **2018**, *11*, 2204. [CrossRef]
8. Stathopoulos, T.; Alrawashdeh, H.; Al-Quraan, A.; Blocken, B.; Dilimulati, A.; Paraschivoiu, M.; Pilay, P. Urban wind energy: Some views on potential and challenges. *J. Wind Eng. Ind. Aerodyn.* **2018**, *179*, 146–157. [CrossRef]
9. Anup, K.C.; Whale, J.; Urmee, T. Urban wind conditions and small wind turbines in the built environment: A review. *Renew. Energy* **2019**, *131*, 268–283. [CrossRef]
10. Tasneem, Z.; Al Noman, A.; Das, S.K.; Saha, D.K.; Islam, R.; Ali, F.; Badal, F.R.; Ahamed, H.; Moyeen, S.I.; Alam, F. An analytical review on the evaluation of wind resource and wind turbine for urban application: Prospect and challenges. *Dev. Built Environ.* **2020**, *4*, 100033. [CrossRef]
11. Reja, R.; Amin, R.; Tasneem, Z.; Ali, F.; Islam, R.; Saha, D.K.; Badal, F.R.; Ahamed, H.; Moyeen, S.I.; Das, S.K. A review of the evaluation of urban wind resources: Challenges and perspectives. *Energy Build.* **2022**, *257*, 111781. [CrossRef]
12. Isyumov, N.; Davenport, A. Comparison of full-scale and wind tunnel wind speed measurements in the commerce court plaza. *J. Ind. Aerodyn.* **1975**, *1*, 201–212. [CrossRef]
13. Murakami, S.; Uehara, K.; Komine, H. Amplification of wind speed at ground level due to construction of high-rise building in urban area. *J. Wind Eng. Ind. Aerodyn.* **1979**, *4*, 343–370. [CrossRef]
14. Wu, H.; Stathopoulos, T. Wind-tunnel techniques for assessment of pedestrian-level winds. *J. Eng. Mech.* **1993**, *119*, 1920–1936. [CrossRef]
15. Eliasson, I.; Offerle, B.; Grimmond, C.; Lindqvist, S. Wind fields and turbulence statistics in an urban street canyon. *Atmos. Environ.* **2006**, *40*, 1–16. [CrossRef]
16. Ricciardelli, F.; Polimeno, S. Some characteristics of the wind flow in the lower Urban Boundary Layer. *J. Wind Eng. Ind. Aerodyn.* **2006**, *94*, 815–832. [CrossRef]
17. Dannecker, R.K.W.; Grant, A.D. Investigations of a building-integrated ducted wind turbine module. *Wind. Energy* **2002**, *5*, 53–71. [CrossRef]
18. Al-Quraan, A.; Stathopoulos, T.; Pillay, P. Comparison of wind tunnel and on site measurements for urban wind energy estimation of potential yield. *J. Wind Eng. Ind. Aerodyn.* **2016**, *158*, 1–10. [CrossRef]
19. Toja-Silva, F.; Kono, T.; Peralta, C.; Lopez-Garcia, O.; Chen, J. A review of computational fluid dynamics (CFD) simulations of the wind flow around buildings for urban wind energy exploitation. *J. Wind Eng. Ind. Aerodyn.* **2018**, *180*, 66–87. [CrossRef]
20. Calautit, K.; Aquino, A.; Calautit, J.K.; Nejat, P.; Jomehzadeh, F.; Hughes, B.R. A Review of Numerical Modelling of Multi-Scale Wind Turbines and Their Environment. *Computation* **2018**, *6*, 24. [CrossRef]
21. Juan, Y.-H.; Rezaeiha, A.; Montazeri, H.; Blocken, B.; Wen, C.-Y.; Yang, A.-S. CFD assessment of wind energy potential for generic high-rise buildings in close proximity: Impact of building arrangement and height. *Appl. Energy* **2022**, *321*, 119328. [CrossRef]
22. Kwok, K.; Hu, G. Wind energy system for buildings in an urban environment. *J. Wind Eng. Ind. Aerodyn.* **2023**, *234*, 105349. [CrossRef]
23. Franke, J.; Hellsten, A.; Schlunzen, H.; Carissimo, B. (Eds.) *Best Practice Guideline for the CFD Simulation of Flows in the Urban Environment—COST Action 732*; COST Office: Brussels, Belgium, 2007; 52p.
24. Tominaga, Y.; Mochida, A.; Yoshie, R.; Kataoka, H.; Nozu, T.; Yoshikawa, M.; Shirasawa, T. AIJ guidelines for practical applications of CFD to pedestrian wind environment around buildings. *J. Wind Eng. Ind. Aerodyn.* **2008**, *96*, 1749–1761. [CrossRef]
25. Blocken, B.; Janssen, W.; van Hooff, T. CFD simulation for pedestrian wind comfort and wind safety in urban areas: General decision framework and case study for the Eindhoven University campus. *Environ. Model. Softw.* **2012**, *30*, 15–34. [CrossRef]
26. Toja-Silva, F.; Peralta, C.; Lopez-Garcia, O.; Navarro, J.; Cruz, I. Roof region dependent wind potential assessment with different RANS turbulence models. *J. Wind Eng. Ind. Aerodyn.* **2015**, *142*, 258–271. [CrossRef]
27. Ruiz, C.A.; Kalkman, I.; Blocken, B. Aerodynamic design optimization of ducted openings through high-rise buildings for wind energy harvesting. *Build. Environ.* **2021**, *202*, 108028. [CrossRef]
28. Yang, A.-S.; Su, Y.-M.; Wen, C.-Y.; Juan, Y.-H.; Wang, W.-S.; Cheng, C.-H. Estimation of wind power generation in dense urban area. *Appl. Energy* **2016**, *171*, 213–230. [CrossRef]
29. Iwashita, H.; Morita, T.; Shibata, K.; Kobayashi, F. Downburst observations by a high density ground surface observation network (POTEKA). *J. Atmos. Electr.* **2019**, *38*, 23–35. [CrossRef]
30. ANSYS Inc. *ANSYS Fluent 2022R1 User's Guide*; ANSYS Inc.: Canonsburg, PA, USA, 2022.
31. Shih, T.-H.; Liou, W.W.; Shabbir, A.; Yang, Z.; Zhu, J. A new k-e eddy viscosity model for high Reynolds number turbulent flows. *Comput. Fluids* **1995**, *24*, 227–238. [CrossRef]
32. Jones, W.; Launder, B. The prediction of laminarization with a two-equation model of turbulence. *Int. J. Heat Mass Transf.* **1972**, *15*, 301–314. [CrossRef]
33. Gromke, C.; Blocken, B. Influence of avenue-trees on air quality at the urban neighborhood scale. Part I: Quality assurance studies and turbulent Schmidt number analysis for RANS CFD simulations. *Environ. Pollut.* **2015**, *196*, 214–223. [CrossRef]
34. Mittal, H.; Sharma, A.; Gairola, A. A review on the study of urban wind at the pedestrian level around buildings. *J. Build. Eng.* **2018**, *18*, 154–163. [CrossRef]

35. Van Druenen, T.; van Hooff, T.; Montazeri, H.; Blocken, B. CFD evaluation of building geometry modifications to reduce pedestrian-level wind speed. *Build. Environ.* **2019**, *163*, 106293. [CrossRef]
36. Shirzadi, M.; Tominaga, Y. Multi-fidelity shape optimization methodology for pedestrian-level wind environment. *Build. Environ.* **2021**, *204*, 108076. [CrossRef]
37. AIJ. *AIJ Recommendations for Loads on Buildings (2015)*; Architectural Institute of Japan: Tokyo, Japan, 2019; ISBN 978-4-8189-5003-0.
38. Launder, B.E.; Spalding, D.B. The numerical computation of turbulent flows. *Comput. Methods Appl. Mech. Eng.* **1974**, *3*, 269–289. [CrossRef]
39. Cebeci, T.; Bradshaw, P. *Momentum Transfer in Boundary Layers*; Hemisphere Publishing Corporation: New York, NY, USA, 1977.
40. Blocken, B.; Stathopoulos, T.; Carmeliet, J. CFD simulation of the atmospheric boundary layer: Wall function problems. *Atmos. Environ.* **2007**, *41*, 238–252. [CrossRef]
41. Hnaien, N.; Hassen, W.; Kolsi, L.; Mesloub, A.; Alghaseb, M.A.; Elkhayat, K.; Abdelhafez, M.H.H. CFD Analysis of Wind Distribution around Buildings in Low-Density Urban Community. *Mathematics* **2022**, *10*, 1118. [CrossRef]
42. Murakami, S. Comparison of various turbulence models applied to a bluff body. *J. Wind Eng. Ind. Aerodyn.* **1993**, *46–47*, 21–36. [CrossRef]
43. Tominaga, Y.; Mochida, A.; Murakami, S.; Sawaki, S. Comparison of various revised k–ε models and LES applied to flow around a high-rise building model with 1:1:2 shape placed within the surface boundary layer. *J. Wind Eng. Ind. Aerodyn.* **2008**, *96*, 389–411. [CrossRef]
44. Tominaga, Y.; Akabayashi, S.-I.; Kitahara, T.; Arinami, Y. Air flow around isolated gable-roof buildings with different roof pitches: Wind tunnel experiments and CFD simulations. *Build. Environ.* **2015**, *84*, 204–213. [CrossRef]
45. Ntinas, G.K.; Shen, X.; Wang, Y.; Zhang, G. Evaluation of CFD turbulence models for simulating external airflow around varied building roof with wind tunnel experiment. *Build. Simul.* **2018**, *11*, 115–123. [CrossRef]
46. Zanforlin, S.; Nishino, T. Fluid dynamic mechanisms of enhanced power generation by closely spaced vertical axis wind turbines. *Renew. Energy* **2016**, *99*, 1213–1226. [CrossRef]
47. Lam, H.; Peng, H. Study of wake characteristics of a vertical axis wind turbine by two- and three-dimensional computational fluid dynamics simulations. *Renew. Energy* **2016**, *90*, 386–398. [CrossRef]
48. Blocken, B.; Stathopoulos, T.; van Beeck, J. Pedestrian-level wind conditions around buildings: Review of wind-tunnel and CFD techniques and their accuracy for wind comfort assessment. *Build. Environ.* **2016**, *100*, 50–81. [CrossRef]
49. Fan, Z.; Zhu, C. The optimization and the application for the wind turbine power-wind speed curve. *Renew. Energy* **2019**, *140*, 52–61. [CrossRef]
50. Bilendo, F.; Meyer, A.; Badihi, H.; Lu, N.; Cambron, P.; Jiang, B. Applications and Modeling Techniques of Wind Turbine Power Curve for Wind Farms—A Review. *Energies* **2023**, *16*, 180. [CrossRef]
51. Jung, J.; Broadwater, R.P. Current status and future advances for wind speed and power forecasting. *Renew. Sustain. Energy Rev.* **2014**, *31*, 762–777. [CrossRef]